Modeling Birkeland currents in the expanding/contracting polar cap paradigm

S. E. Milan [1,2]

Received 16 October 2012; revised 1 May 2013; accepted 11 June 2013; published 9 September 2013.

[1] We present a simple mathematical model of the region 1 and 2 Birkeland current system intensities for differing dayside and nightside magnetic reconnection rates, consistent with the expanding/contracting polar cap paradigm of solar wind-magnetosphere-ionosphere coupling. The current intensities are shown to be dependent on the cross-polar cap potential, which is the average of the dayside and nightside reconnection rates. Current intensities are expected to maximize on the dayside or the nightside when magnetopause or magnetotail reconnection dominates. Current intensities are also dependent on the ionospheric conductance, the width of the merging gaps, the width of the ionospheric convection return flow region, and on the size of the polar cap.

Citation: Milan, S. E. (2013), Modeling Birkeland currents in the expanding/contracting polar cap paradigm, *J. Geophys. Res. Space Physics*, *118*, 5532–5542, doi:10.1002/jgra.50393.

1. Introduction

[2] The substorm cycle is a key component of the dynamics of the magnetosphere, representing the cycle of interconnection and release of interplanetary magnetic field lines with the terrestrial field by magnetic reconnection. This cycle drives a circulation of plasma in the magnetosphere, which is communicated to the ionosphere via magnetic field-aligned currents, the existence of which was first proposed by *Birkeland* [1908]. In this paper, we outline a simple model that allows the Birkeland current intensities to be estimated from an understanding of the nonsteady nature of solar wind-magnetosphere coupling.

[3] Building on Dungey's model of solar wind-magnetosphere coupling [*Dungey*, 1961, 1963], the expanding/contracting polar cap paradigm (ECPC) [*Cowley and Lockwood*, 1992; *Lockwood and Cowley*, 1992] provides a quantitative means of describing changes in the proportion of the magnetic flux associated with the terrestrial dipole that is interconnected with interplanetary space (open flux) under the action of magnetic reconnection at the magnetopause and in the magnetotail. The open flux, also known as the polar cap flux, F_{PC}, varies as

$$\frac{\mathrm{d}F_{\mathrm{PC}}}{\mathrm{d}t} = \Phi_D - \Phi_N \tag{1}$$

where Φ_D and Φ_N are the rates of dayside and nightside reconnection, that is, reconnection between the interplanetary magnetic field (IMF) and the magnetopause, and between open field lines of the northern and southern magnetotail lobes. The dayside rate is dependent on conditions in the interplanetary medium, in particular, the solar wind speed and the strength and orientation of the IMF [e.g., *Milan et al.*, 2012, and references therein]. The nightside rate is linked primarily to the occurrence of substorm processes [e.g., *Lockwood and Cowley*, 1992; *Milan et al.*, 2007].

[4] The primary prediction of the ECPC paradigm is that when dayside reconnection dominates over nightside reconnection, the polar cap expands and the auroras move to lower latitudes, and as the nightside reconnection grows to dominate over the dayside rate, the polar cap contracts, known as the substorm "growth" and "expansion" phases, respectively [*Rostoker et al.*, 1980]. The ECPC also gives a qualitative way to understand the excitation of magnetospheric and ionospheric convection in response to changes in open flux [*Cowley and Lockwood*, 1992; *Milan et al.*, 2003; *Chisham et al.*, 2008]. Under specific assumptions about the shape of the polar cap or open/closed field line boundary (OCB), it is possible to derive analytic expressions for the ionospheric convection electrostatic potential associated with changes in F_{PC} [e.g., *Siscoe and Huang*, 1985; *Freeman*, 2003; *Milan et al.*, 2012].

[5] Viewed from a different perspective, convective motions are driven by stresses at the magnetopause communicated to the ionosphere by field-aligned currents (FACs) known as Birkeland currents [*Birkeland*, 1908]. As deduced in the 1960s and 1970s, these FACs form two concentric rings around each pole, an inner ring (region 1 or R1) which connects to the magnetopause and tail currents and an outer ring (region 2 or R2) which feeds the partial ring current [e.g., *Iijima and Potemra*, 1976a, 1976b, 1978; *Cowley*, 2000, and references therein]. These FACs can be measured as magnetic perturbations detected by spacecraft as they traverse the currents (originally *Zmuda et al.* [1966]; see also *Fujii et al.* [1994] and *Hoffman et al.* [1994]), as the divergence of horizontal currents in the ionosphere [e.g., *Opgenoorth et al.*, 1980; *Amm*, 1995], or as vorticity in the ionospheric convection pattern [e.g., *Sofko et al.*, 1995; *McWilliams*, 1997;

[1]Department of Physics and Astronomy, University of Leicester, Leicester, UK.
[2]Birkeland Centre for Space Science, Bergen, Norway.

Corresponding author: S. E. Milan, Department of Physics and Astronomy, University of Leicester, Leicester LE1 7RH, UK. (steve.milan@ion.le.ac.uk)

2169-9380/13/10.1002/jgra.50393

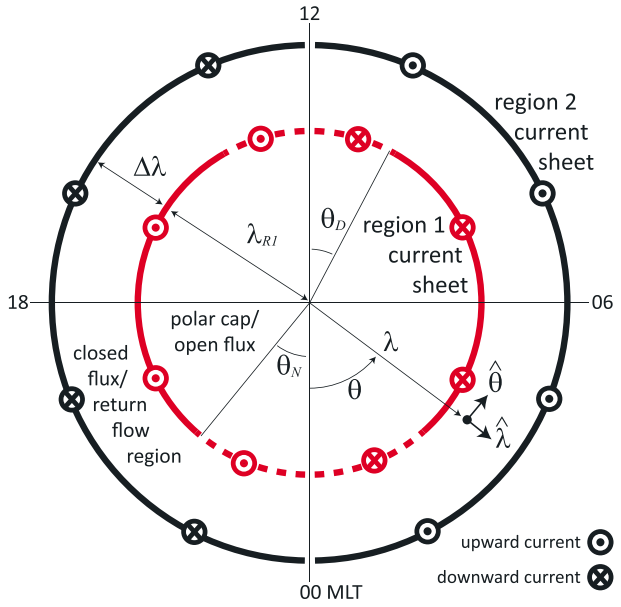

Figure 1. A schematic diagram of the main features of the model. The region 1 (R1) and region 2 (R2) current sheets are idealized to thin sheets whose footprints in the ionosphere form concentric rings centered on the geomagnetic pole. A general point has colatitude λ and azimuth θ (measured from midnight). The R1 ring (red) is identified with the open/closed field line boundary (OCB) and is located at colatitude λ_{R1}. The dayside and nightside merging gaps (shown as dashed portions of the OCB) have half-widths of θ_D and θ_N, respectively. The R2 current ring is located at a colatitude of $\lambda_{R2} = \lambda_{R1} + \Delta\lambda$. The region inside the OCB is known as the polar cap (PC) region and is treaded by the open field lines of the magnetotail lobes, comprising magnetic flux F_{PC}. Equatorward of the OCB, magnetic flux is closed. The region between the R1 and R2 ovals is known as the return flow (RF) region, and can be loosely identified with the auroral zone. The model assumes ionospheric conductances of Σ_{PC} and Σ_{RF} in the polar cap and return flow regions, respectively. The sense of the currents flowing in the dawn and dusk portions of the R1 and R2 rings are indicated by arrows outward and into the page.

Chisham et al., 2009]. In the Northern Hemisphere, current flows into (out of) the ionosphere in the R1 dawn (dusk) sector and the R2 dusk (dawn) sector, as depicted in Figure 1. The total current flowing into and out of the ionosphere typically amounts to several mega-amps (MA). Empirical models of the FAC systems have been developed and parameterized by interplanetary conditions [e.g., *Weimer*, 2005; *Anderson et al.*, 2008; *He et al.*, 2012], indicating that the currents are dependent on the level of geomagnetic activity driven by enhanced solar wind-magnetosphere coupling, as first deduced by *Iijima and Potemra* [1978].

[6] Recently, the Active Magnetosphere and Planetary Electrodynamics Experiment (AMPERE) technique has allowed the FAC patterns to be imaged globally at a cadence of 10 min [e.g., *Anderson et al.*, 2000, 2002; *Clausen et al.*, 2012]. At these temporal scales, it has become clear that the locations of the R1 and R2 FACs respond to interplanetary conditions in a way that is consistent with the ECPC, moving to lower latitudes when dayside reconnection dominates and contracting poleward when nightside reconnection is dominant [*Clausen et al.*, 2012]. However, there currently lacks an understanding of how the magnitude of the currents should vary with differing reconnection rates or through a substorm cycle. Having said this, the ECPC modeling mentioned above [*Siscoe and Huang*, 1985; *Freeman*, 2003; *Milan et al.*, 2012] is based on the assumption of current continuity between horizontal ionospheric currents associated with convection and the R1/R2 FAC system, but the magnitude of the current systems is not explicitly calculated. In this paper, we extend these models to provide estimates of the current for differing dayside and nightside reconnection rates. Such estimates will be useful for future studies comparing with observed currents.

2. The Model

[7] On time scales longer than a few 10 s, the magnetic field in the ionosphere can be considered stationary, which implies by Faraday's law that the electric field **E** associated with plasma convective motions is irrotational and can be expressed as an electrostatic potential Φ, such that

$$\mathbf{E} = -\nabla\Phi. \tag{2}$$

[8] The current flowing in the ionosphere, perpendicular to the magnetic field, is related to the electric field by

$$\mathbf{J}_\perp = \Sigma_P \mathbf{E} + \Sigma_H \hat{\mathbf{B}} \times \mathbf{E}, \tag{3}$$

where $\hat{\mathbf{B}}$ is the unit vector of the magnetic field and Σ_P and Σ_H are the height-integrated Pedersen and Hall conductivities. Divergence of this current must be accompanied by field-aligned currents into or out of the ionosphere, $j_{||}$, such that

$$j_{||} = \nabla\cdot\mathbf{J}_\perp = \Sigma_P \nabla^2\Phi + \nabla\Phi\cdot\nabla\,\Sigma_P + \left(\nabla\Phi \times \hat{\mathbf{B}}\right)\cdot\nabla\,\Sigma_H. \tag{4}$$

[9] We will refer to the three terms on the right-hand side (RHS) of equation (4) as terms 1, 2, and 3. Term 1 relates to the divergence of the Pedersen current due to divergence of the convection electric field, term 2 to divergence of the Pedersen current due to gradients in the Pedersen conductivity along the direction in which the Pedersen current flows, and term 3 to divergence of the Hall current due to gradients in the Hall conductivity along the direction that the Hall current flows.

[10] Our model computes Φ based on the ECPC convection model successively developed by *Siscoe and Huang* [1985], *Freeman and Southwood* [1988], *Freeman* [2003], and *Milan et al.* [2012]. It then uses simple assumptions regarding the spatial distributions of Σ_P and Σ_H to determine $j_{||}$ from equation (4). The convection model divides the polar ionosphere into three regions or domains, as indicated in Figure 1: the polar cap in which antisunward plasma drift occurs, the return flow region in which predominantly sunward plasma drift occurs, and a low-latitude region in which no convective motion occurs. The boundaries between these domains are associated with significant convection shears, which contribute to term 1 of equation (4). Furthermore, we identify the return flow region with the auroral zone, in which auroral precipitation occurs to increase

Table 1. Functional Form of Φ_{R1}

θ	$\Phi_{R1}(\theta) =$
$0 < \theta < \theta_N$	$-R_E \sin\lambda_{R1}\{E_N\theta\}$
$\theta_N < \theta < \pi - \theta_D$	$-R_E \sin\lambda_{R1}\{(E_N - E_B)\theta_N + E_B\theta\}$
$\pi - \theta_D < \theta < \pi + \theta_D$	$-R_E \sin\lambda_{R1}\{(E_N - E_B)\theta_N + (E_D - E_B)(\theta_D - \pi) + E_D\theta\}$
$\pi + \theta_D < \theta < 2\pi - \theta_N$	$-R_E \sin\lambda_{R1}\{(E_N - E_B)\theta_N + 2(E_D - E_B)\theta_D + E_B\theta\}$
$2\pi - \theta_N < \theta < 2\pi$	$-R_E \sin\lambda_{R1}\{2(E_N - E_B)(\theta_N - \pi) + 2(E_D - E_B)\theta_D + E_N\theta\}$

the ionospheric conductivity. In other words, the boundaries of the convection model are also the locations where significant gradients in the conductivities are expected to arise, contributing to terms 2 and 3 of equation (4). These two factors indicate that the Birkeland currents in our model are confined to the boundaries of the convection model domains, that is, region 1 currents form a ring at the polar cap boundary or open/closed field line boundary (OCB), and the region 2 currents form a ring at the low-latitude boundary of the convection pattern. Both current rings are assumed sufficiently thin that their latitudinal extent can be neglected.

[11] A simplifying assumption of the model is that the conductivity is uniform in the polar cap and is uniform in the return flow region, though it is expected to be higher in the latter. As the Birkeland currents are confined to the boundaries of the three domains of the convection model, and as the conductivity is spatially uniform within the domains themselves, equation (4) reduces to

$$\nabla^2\Phi = 0 \tag{5}$$

at all points away from the domain boundaries themselves. Hence, the convection electrostatic potential is determined from a solution of Laplace's equation in each of the three domains, subject to boundary conditions on the potential dictated by the dayside and nightside reconnection rates and expansions and contractions of the convection pattern (see below). That is, the problem is identical to solving the electrostatic potential due to localized electric charges in regions not including the charges. Once the electrostatic potential is known, the Birkeland currents can be computed by determining the current flowing into or out of each of the domains around their boundaries, using equation (4).

[12] We assume that the Earth's surface is spherical, and measure positions in terms of magnetic colatitude λ and magnetic azimuth θ, where $\theta = 0$ is defined as magnetic local midnight (00 MLT) and is measured in the same sense as magnetic local time, such that $\theta = \pi/2$ represents 06 MLT (see Figure 1). The potential and electric field can be represented as $\Phi(\theta,\lambda)$ and $\mathbf{E}(\theta,\lambda) = E_\theta\hat{\boldsymbol{\theta}} + E_\lambda\hat{\boldsymbol{\lambda}}$, where $\hat{\boldsymbol{\theta}}$ and $\hat{\boldsymbol{\lambda}}$ are positive in the sense of increasing MLT and equatorward, respectively. To be specific, in the Northern Hemisphere, **B** points into the Earth. We assume that the Earth's magnetic field, **B**, is dipolar, such that the radial component at the Earth surface is given by

$$B_r(\lambda) = 2B_{eq}\cos\lambda, \tag{6}$$

where B_{eq} is the equatorial field strength of 31,000 nT.

[13] The open magnetic flux of the magnetosphere is equal to this radial component integrated over the area of the polar cap

$$F_{PC} = \int_{PC} \mathbf{B}\cdot\mathbf{ds}. \tag{7}$$

[14] We assume that the polar cap is circular and centered on the geomagnetic pole, and that the region 1 current system is colocated with the open/closed field line boundary (OCB) at a colatitude λ_{R1}. In this case, the open magnetic flux contained within the polar cap is given by

$$F_{PC} = 2\pi R_E^2 B_{eq}\sin^2\lambda_{R1}. \tag{8}$$

[15] This allows λ_{R1} to be determined for a given value of F_{PC}. Changes in the amount of open flux through equation (1) imply that λ_{R1} must vary, and the OCB and R1 current oval move with a speed (positive equatorward)

$$V_{R1} = R_E\frac{d\lambda_{R1}}{dt} = \frac{(\Phi_D - \Phi_N)}{2\pi R_E^2 B_{eq}\sin 2\lambda_{R1}}. \tag{9}$$

[16] Along "adiaroic" portions of the OCB, the plasma and boundary move together; there is flow of plasma across the boundary only at the merging gaps (Figure 1, dashed lines) [e.g., *Siscoe and Huang*, 1985]. The dayside and nightside merging gaps have angular half-widths of θ_D and θ_N, centered at $\theta = \pi$ and $\theta = 0$, having lengths $l_D = 2\theta_D R_E\sin\lambda_{R1}$ and $l_N = 2\theta_N R_E\sin\lambda_{R1}$, respectively. Flow is considered to be perpendicular to the OCB at all θ, so that the electric field perpendicular to the boundary is

$$E_\lambda(\lambda_{R1},\theta) = 0. \tag{10}$$

[17] From $\mathbf{E} = -\mathbf{V}\times\mathbf{B}$, the parallel component of the electric field around nonreconnecting portions of the boundary is

$$E_\theta(\lambda_{R1},\theta) = E_B = -V_{R1}B_r,\ \theta_N < |\theta| < \pi - \theta_D. \tag{11}$$

[18] At the merging gaps, in the frame of the moving boundary, the electric field associated with magnetic flux transfer across the boundary (due to reconnection) is Φ_D/l_D and Φ_N/l_N, which in the frame of the Earth becomes

$$E_\theta(\lambda_{R1},\theta) = E_D = -V_{R1}B_r + \Phi_D/l_D,\ |\theta| > \pi - \theta_D, \tag{12}$$

and

$$E_\theta(\lambda_{R1},\theta) = E_N = -V_{R1}B_r - \Phi_N/l_N,\ |\theta| < \theta_N. \tag{13}$$

[19] Integrating E_θ around the boundary gives the potential at the region 1 current system, $\Phi_{R1}(\theta) = \Phi(\lambda_{R1},\theta)$, as a function of azimuth:

$$\Phi_{R1}(\theta) = -R_E\sin\lambda_{R1}\int_0^\theta E_\theta(\lambda_{R1},\theta)d\theta. \tag{14}$$

[20] Table 1 tabulates the functional form of $\Phi_{R1}(\theta)$ at different azimuths, derived from equations (11)–(14). By way of example, Figures 2a and 2b show the variation of Φ_{R1} as a function of MLT for two cases: (a) $\Phi_D = 50$ kV,

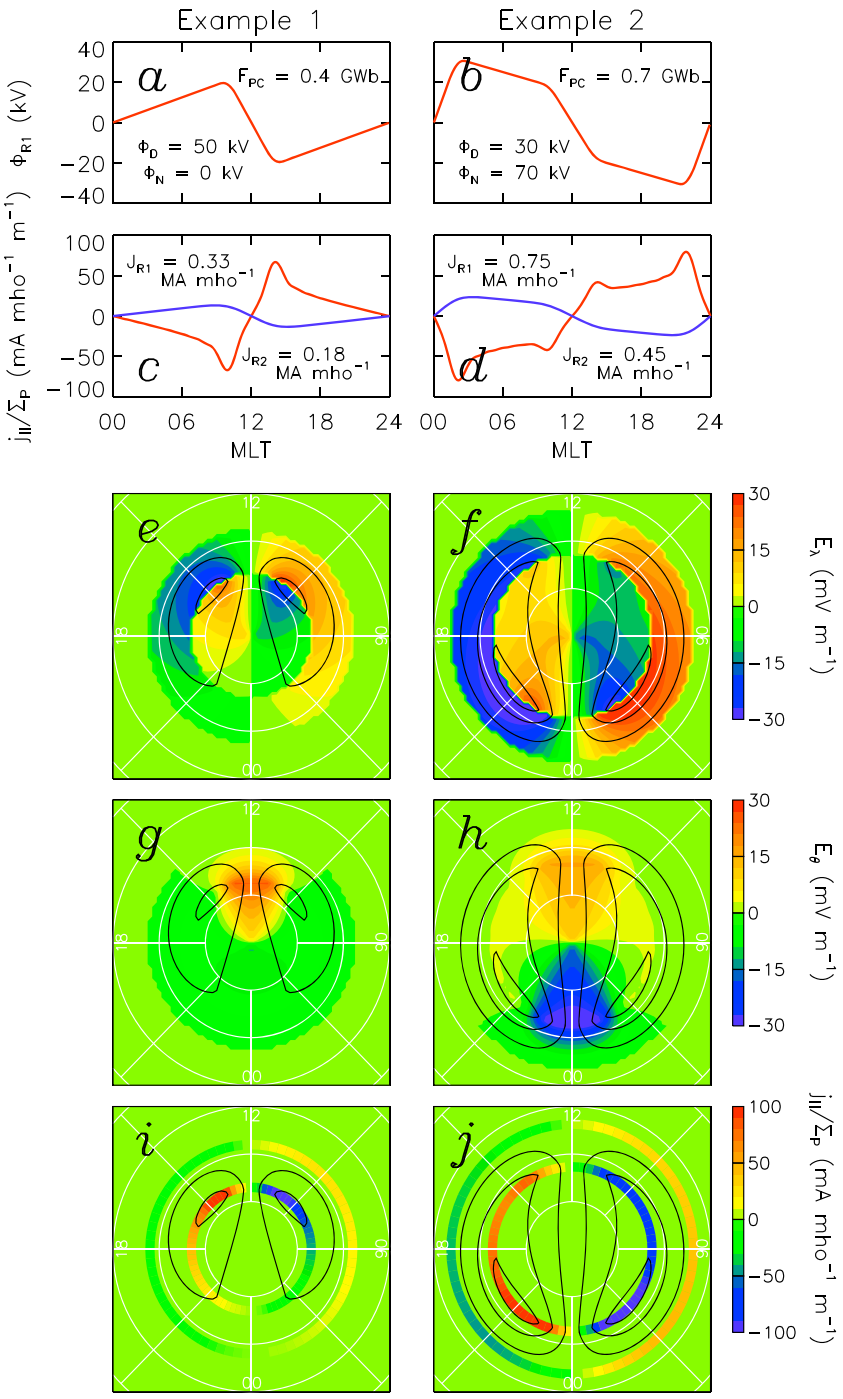

Figure 2. Output of the model for two scenarios: example 1, $\Phi_D = 50$ kV, $\Phi_N = 0$ kV, $F_{PC} = 0.4$ GWb; example 2, $\Phi_D = 30$ kV, $\Phi_N = 70$ kV, $F_{PC} = 0.7$ GWb; in both cases, $\theta_D = \theta_N = 30°$, $\Delta\lambda = 10°$, $\Sigma_{PC} = \Sigma_{RF} = 1$ mho. (a and b) The magnetic local time variation of the polar cap boundary potential Φ_{R1}. (c and d) The MLT variation of the R1 and R2 current intensities j_{R1} (red) and j_{R2} (blue). The total R1 and R2 currents J_{R1} and J_{R2} are shown in the corners. (e and f) The meridional component of the ionospheric convection electric field component E_λ, presented on a magnetic latitude and MLT grid, concentric circles showing 10° intervals of latitude. The convection electric potential Φ is overlaid as black contours, with contours shown at 6 kV intervals. (g and h) Similar to Figures 2e and 2f except for the azimuthal electric field E_θ component. (i and j) The upward and downward current intensities j_{R1} and j_{R2}; note that for clarity these have been shown of nonzero latitudinal width.

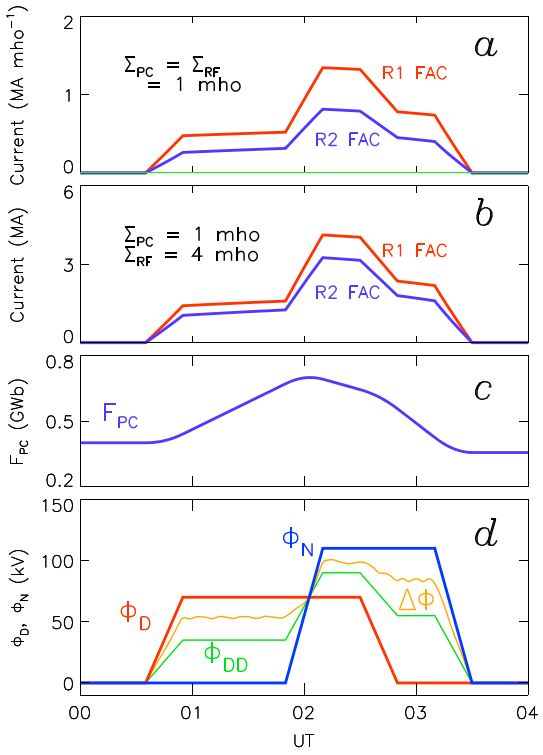

Figure 3. Time series of the dayside and nightside reconnection rates, polar cap flux, and current intensities for a simulated substorm cycle. (a) The region 1 and 2 current strengths J_{R1} and J_{R2} for $\Sigma_{PC}=1$ mho and $\Sigma_{RF}=4$ mho. (b) J_{R1} and J_{R2} for $\Sigma_{PC}=\Sigma_{RF}=1$ mho. (c) The variation in polar cap flux F_{PC}. (d) The dayside and nightside reconnection rates Φ_D (red) and Φ_N (blue) that drive convection and the field-aligned currents. Also shown are the maximum potential difference in the convection pattern $\Delta\Phi$ (green) and the potential difference across the dawn-dusk meridian Φ_{DD} (orange), two different measures of the cross-polar cap potential.

$\Phi_N=0$, $F_{PC}=0.4$ GWb and (b) $\Phi_D=30$ kV, $\Phi_N=70$ kV, $F_{PC}=0.7$ GWb. In both cases, we have used $\theta_D=\theta_N=\pi/6$ (30°).

[21] The R2 FAC is placed at some distance $\Delta\lambda$ equatorward of the R1 current, $\lambda_{R2}=\lambda_{R1}+\Delta\lambda$. In the low-latitude domain of the problem, at $\lambda\geq\lambda_{R2}$, there is no convection, so

$$\Phi_{R2}(\theta)=\Phi(\lambda_{R2},\theta)=0. \tag{15}$$

In the examples shown in Figure 2, we use $\Delta\lambda=\pi/18$ (10°).

[22] Φ_{R1} and Φ_{R2} are the boundary conditions used for solution of equation (5). The full solution comprises the three domains discussed previously: $\lambda<\lambda_{R1}$, which we term the polar cap (PC) region, $\lambda_{R1}<\lambda<\lambda_{R2}$, the return flow (RF) region, and $\lambda>\lambda_{R2}$, the low-latitude (LL) region. As shown by *Freeman* [2003], the solution is facilitated by use of the substitution $\Lambda=\log_e\tan\frac{1}{2}\lambda$ (note $d\Lambda/d\lambda=(\sin\lambda)^{-1}$), in which case, equation (5) becomes

$$\nabla^2\Phi=\frac{\partial^2\Phi}{\partial\Lambda^2}+\frac{\partial^2\Phi}{\partial\theta^2}=0. \tag{16}$$

[23] Solutions of equation (16) in the different regions are then

$$\Phi_{PC}(\Lambda,\theta)=\sum_{m=1}^{N}s_m\sin m\theta\exp m(\Lambda-\Lambda_{R1}), \tag{17}$$

$$\Phi_{RF}(\Lambda,\theta)=\sum_{m=1}^{N}s_m\sin m\theta\frac{\sinh m(\Lambda-\Lambda_{R2})}{\sinh m(\Lambda_{R1}-\Lambda_{R2})}, \tag{18}$$

$$\Phi_{LL}(\Lambda,\theta)=0. \tag{19}$$

[24] In equations (17) and (18), s_m are coefficients of a Fourier expansion of Φ_{R1}, which for ease of computation, we truncate at order N; $N=20$ has been used in subsequent calculations. s_m can be found from

$$s_m=\frac{1}{\pi}\int_0^{2\pi}\Phi_{R1}(\theta)\sin m\theta\,d\theta; \tag{20}$$

the function Φ_{R1} is odd, so cosine terms, c_m, do not appear in the Fourier transform and hence do not appear in equations (17) and (18). Alternatively, s_m can be determined analytically from the functional form of Φ_{R1} described in Table 1, which after some manipulation yields

$$s_m=-\frac{1}{m^2\pi}\left\{(-1)^m\frac{\Phi_D\sin m\theta_D}{\theta_D}-\frac{\Phi_N\sin m\theta_N}{\theta_N}\right\}. \tag{21}$$

[25] Equipotential contours of Φ, derived from equations (17) and (18), are streamlines of the ionospheric flow. Figures 2e–2j show equipotentials for cases a and b described above, contoured with a spacing of 6 kV. In both cases, the twin-cell convection pattern is apparent. In case a, this is associated with an expanding polar cap as $\Phi_D>\Phi_N$; the situation is reversed in case b.

[26] To fully characterize the flow, we determine the associated electric field from equation (2). To do this, we require the following results:

$$\frac{\partial\Phi_{PC}}{\partial\Lambda}(\Lambda,\theta)=\sum_{m=1}^{N}s_m m\sin m\theta\exp m(\Lambda-\Lambda_{R1}), \tag{22}$$

$$\frac{\partial\Phi_{PC}}{\partial\theta}(\Lambda,\theta)=\sum_{m=1}^{N}s_m m\cos m\theta\exp m(\Lambda-\Lambda_{R1}), \tag{23}$$

$$\frac{\partial\Phi_{RF}}{\partial\Lambda}(\Lambda,\theta)=\sum_{m=1}^{N}s_m m\sin m\theta\frac{\cosh m(\Lambda-\Lambda_{R2})}{\sinh m(\Lambda_{R1}-\Lambda_{R2})}, \tag{24}$$

and

$$\frac{\partial\Phi_{RF}}{\partial\theta}(\Lambda,\theta)=\sum_{m=1}^{N}s_m m\cos m\theta\frac{\sinh m(\Lambda-\Lambda_{R2})}{\sinh m(\Lambda_{R1}-\Lambda_{R2})}. \tag{25}$$

[27] Then the electric field in V m^{-1} has components:

$$E_\lambda=-\frac{1}{R_E\sin\lambda}\frac{\partial\Phi}{\partial\Lambda},\text{L}\,E_\theta=-\frac{1}{R_E\sin\lambda}\frac{\partial\Phi}{\partial\theta}, \tag{26}$$

where equations (22) and (23) are used within the polar cap region, and equations (24) and (25) within the return flow region. E_λ and E_θ are contoured in color in Figures 2e–2h

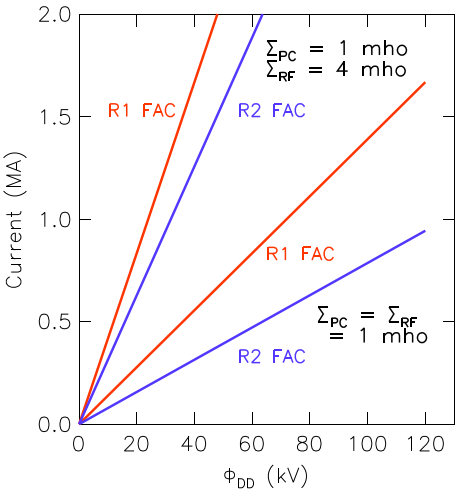

Figure 4. The variation of the region 1 and 2 current strengths J_{R1} and J_{R2} as a function of cross-polar cap potential Φ_{DD} for the cases $\Sigma_{PC}=1$ mho and $\Sigma_{RF}=4$ mho, and $\Sigma_{PC}=\Sigma_{RF}=1$ mho. $F_{PC}=0.5$ GWb, $\theta_D=\theta_N=30°$, $\Delta\lambda=9°$.

for cases a and b. From $\mathbf{V}=\mathbf{E}\times\mathbf{B}/B^2$, the horizontal components of the ionospheric flow vector are

$$V_\lambda = -E_\theta/B_r,\ V_\theta = E_\lambda/B_r. \tag{27}$$

[28] We now derive the field-aligned currents flowing in the R1 and R2 regions from the currents flowing into and out of the convection domains around their boundaries. As described above, we allow the Pedersen conductance, Σ_P, to be different (but uniform) in the polar cap and return flow regions, Σ_{PC} and Σ_{RF}, respectively. We let α be the ratio between Σ_{RF} and Σ_{PC}, such that we can write $\Sigma_{RF}=\alpha\Sigma_{PC}$. Despite a step in conductance between the PC and RF regions, equation (10) requires that term 3 of equation (4) is zero at all points around the boundaries and only the Pedersen current contributes. Then, the R1 field-aligned current is equal to the sum of the Pedersen currents flowing at the boundary of the PC and RF regions at colatitude λ_{R1}; similarly, the R2 FAC is equal to the Pedersen current flowing in the RF region boundary at colatitude λ_{R2} (no current flows in the LL region). For the region 1 system, we have the azimuthal variation in current per unit of azimuthal distance (A m^{-1}):

$$\begin{aligned} j_{R1}(\theta) &= \frac{1}{R_E \sin\lambda_{R1}}\left\{ \Sigma_{RF}\frac{\partial\Phi_{RF}}{\partial\Lambda}(\Lambda_{R1},\theta) - \Sigma_{PC}\frac{\partial\Phi_{PC}}{\partial\Lambda}(\Lambda_{R1},\theta)\right\} \\ &= \frac{\Sigma_{PC}}{R_E \sin\lambda_{R1}}\sum_{m=1}^{N} s_m m \sin m\theta\{\alpha\coth m(\Lambda_{R1}-\Lambda_{R2})-1\}. \end{aligned} \tag{28}$$

[29] Similarly for region 2,

$$\begin{aligned} j_{R2}(\theta) &= -\frac{\Sigma_{RF}}{R_E \sin\lambda_{R2}}\frac{\partial\Phi_{RF}}{\partial\Lambda}(\Lambda_{R2},\theta) \\ &= -\frac{\alpha\Sigma_{PC}}{R_E \sin\lambda_{R2}}\sum_{m=1}^{N} s_m m \sin m\theta\,\mathrm{csch}\, m(\Lambda_{R1}-\Lambda_{R2}). \end{aligned} \tag{29}$$

[30] Figures 2c and 2d show the azimuthal variation in the magnitude of j_{R1}/Σ_P and j_{R2}/Σ_P for cases a and b, in which case it is assumed that $\Sigma_P=\Sigma_{RF}=\Sigma_{PC}=1$ mho. The vertical currents are also indicated in Figures 2i and 2j; note that the current sheets have been plotted of finite width for clarity, whereas in the model, they are idealized to be of zero width.

[31] The second term of the RHS of equation (16) indicates that there is a contribution to the FACs from azimuthal divergence of the electric field. At the R2 FAC, the electric field is zero (equation (15)), so this contribution is zero. At the R1 FAC, the electric field is spatially uniform in azimuth (equations (11)–(13)), such that there is no contribution to the FAC, except at the edges of the merging gaps. At these points, the sense of the discontinuity in electric field is such as to increase the magnitude of the FAC calculated from equation (28). In fact, because of the assumption that the current sheets are infinitely thin, this additional current naturally appears in equation (28): The significance of each term of the summation is multiplied by a factor of m over the components of the Fourier transform of Φ_{R1} (equation (21)), enhancing the contribution of higher-order terms in j_{R1}. These terms result in peaks in the R1 current at the edges of the merging gaps (seen in Figures 2c and 2d). The assumed form of Φ_{R1} has discontinuities in gradient at the edges of the merging gaps, so these enhanced current regions are of infinite intensity, but are of zero azimuthal width. To counteract this, we can terminate the summation in equation (28) at finite N (i.e., $N=20$), or somewhat smooth Φ_{R1}, before taking the Fourier transform (equation (20)). In Figure 2, we have used the latter technique (see Figures 2a and 2b).

[32] As can be seen from Figures 2c, 2d, 2i, and 2j, the region 1 (and to a lesser extent, region 2) current maximizes at the edges of the most active merging gap, i.e., where the vorticity of the ionospheric plasma drift is greatest. That is, when the dayside reconnection rate dominates and the polar cap is expanding, the R1 current is greatest on the dayside, and when the polar cap is contracting, the current maximizes on the nightside.

[33] Finally, we find expressions for the total current flowing in the R1 and R2 FACs, by integrating equations (28) and (29) in azimuth. We define these as the R1 current flowing out of the dawn sector and R2 current flowing into

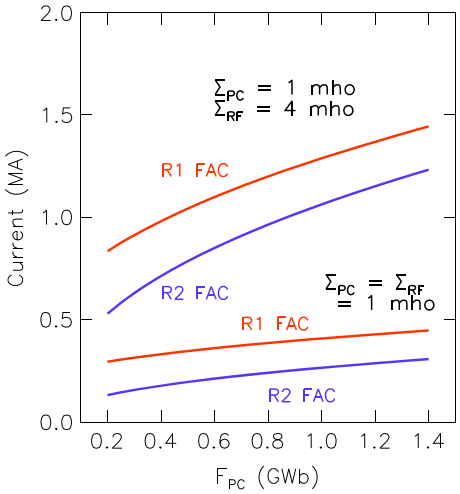

Figure 5. The variation of the region 1 and 2 current strengths J_{R1} and J_{R2} as a function of polar cap flux F_{PC} for the cases $\Sigma_{PC}=1$ mho and $\Sigma_{RF}=4$ mho, and $\Sigma_{PC}=\Sigma_{RF}=1$ mho. $\Phi_{DD}=25$ kV, $\theta_D=\theta_N=30°$, $\Delta\lambda=9°$.

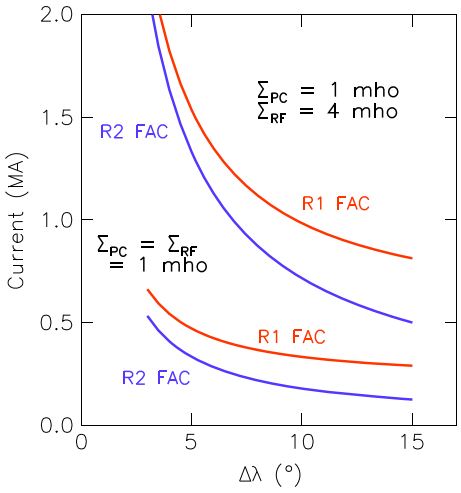

Figure 6. The variation of the region 1 and 2 current strengths J_{R1} and J_{R2} as a function of return flow width $\Delta\lambda$ for the cases $\Sigma_{PC}=1$ mho and $\Sigma_{RF}=4$ mho, and $\Sigma_{PC}=\Sigma_{RF}=1$ mho. $\Phi_{DD}=25$ kV, $F_{PC}=0.5$ GWb, $\theta_D=\theta_N=30°$.

the dawn sector. Our model is symmetric about the noon-midnight meridian, so the currents are equal and opposite in the dusk sector. Hence,

$$J_{R1} = \pi R_E \sin\lambda_{R1} \int_0^{\pi} j_{R1}\,d\theta$$
$$= -2\pi\Sigma_{PC} \sum_{m=1,3,5\ldots}^{N} s_m\{\alpha \coth m(\Lambda_{R1}-\Lambda_{R2}) - 1\} \quad (30)$$

and

$$J_{R2} = \pi R_E \sin\lambda_{R2} \int_0^{\pi} j_{R2}\,d\theta$$
$$= -2\pi\alpha\Sigma_{PC} \sum_{m=1,3,5\ldots}^{N} s_m \operatorname{csch} m(\Lambda_{R1}-\Lambda_{R2}). \quad (31)$$

[34] Note that during integration, even terms in $\sin m\theta$ disappear and only odd terms in s_m remain.

[35] The total R1 and R2 currents (per unit conductance) are indicated in Figures 2c and 2d. If a uniform Pedersen conductivity of 2 mho is assumed across the polar region, then in Example 1, 1.2 and 0.7 MA flow in the R1 and R2 FACs; in Example 2, these are 2.9 and 1.7 MA. The variation in current intensity with differing conditions is explored in section 3.

[36] Finally, we note that the model allows the associated Joule heating rate to be computed. Assuming that neutral winds are negligible, the local Joule heating rate is

$$Q_{JH} = \Sigma_P E^2 = \Sigma_P\left(E_\lambda^2 + E_\theta^2\right), \quad (32)$$

where E_λ and E_θ are found from equation (26). This can be integrated over the PC and RF regions to give the global heating rate.

3. Model Results

[37] The model outlined in section 2 allows the spatial distribution of electrostatic potential, Φ, electric field, **E**, ionospheric flow vector, **V**, region 1 and 2 (R1 and R2) current densities as a function of azimuth, j_{R1} and j_{R2}, and total R1 and R2 current magnitudes, J_{R1} and J_{R2}, to be calculated as a function of dayside and nightside reconnection rates, Φ_D and Φ_N, and polar cap flux, F_{PC}. The model can be configured with different dayside and nightside merging gap (convection throat) widths, θ_D and θ_N, latitudinal offset between R1 and R2 current systems, $\Delta\lambda$, and conductances in the return flow (auroral zone) and polar cap ionospheres, Σ_{RF} and Σ_{PC}. In this section, we explore the predicted current configurations for a range of reconnection rates and simulated episodes of solar wind-magnetosphere coupling.

[38] Figure 3d shows two synthesized time series of dayside and nightside reconnection rates, Φ_D and Φ_N, representing an idealized substorm cycle. At the start of the 4 h interval, the open flux of the magnetosphere stands at 0.4 GWb (Figure 3c). At this time, $\Phi_D=\Phi_N=0$, simulating a period when the interplanetary magnetic field (IMF) is directed northward, so no (low latitude) dayside reconnection is occurring, and no reconnection is occurring in the magnetotail. At 00:40 UT, Φ_D begins to ramp up, reaching 70 kV by 01:00 UT, simulating a southward turning of the IMF, and F_{PC} begins to increase as dictated by equation (1), the substorm growth phase. Around 02:00 UT, Φ_N increases to 110 kV, indicating substorm expansion phase onset. Between 02:00 and 02:30 UT, as $\Phi_N > \Phi_D$, F_{PC} decreases. After 02:30 UT, the rate of contraction of the polar cap increases as the IMF turns northward, $\Phi_D=0$. Nightside reconnection ceases by 03:30 UT.

[39] As well as the dayside and nightside reconnection rates, there are two measures of the strength of the magnetic flux throughput of the magnetosphere, both often called the cross-polar cap potential or transpolar voltage. The first quantifies the rate of antisunward magnetic flux

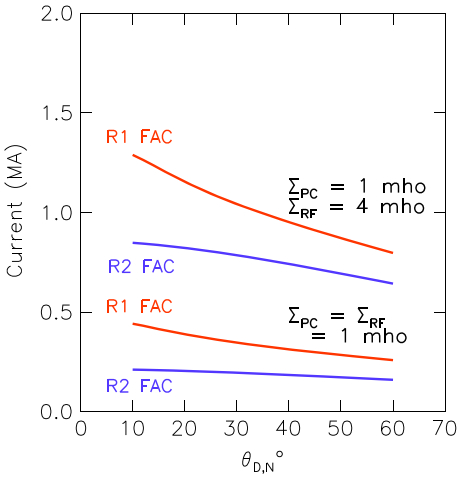

Figure 7. The variation of the region 1 and 2 current strengths J_{R1} and J_{R2} as a function of merging gap half-width θ_D and θ_N, where both are assumed equal, for the cases $\Sigma_{PC}=1$ mho and $\Sigma_{RF}=4$ mho, and $\Sigma_{PC}=\Sigma_{RF}=1$ mho. $\Phi_{DD}=25$ kV, $F_{PC}=0.5$ GWb, $\Delta\lambda=9°$.

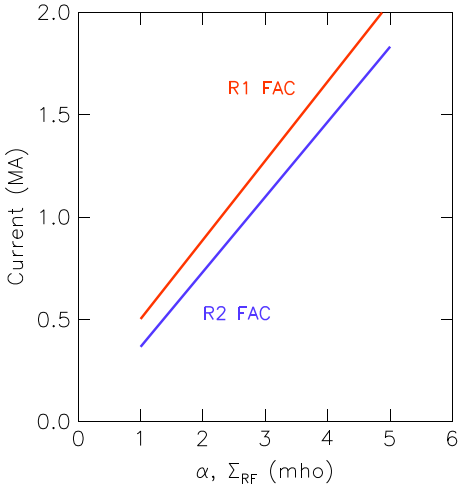

Figure 8. The variation of the region 1 and 2 current strengths J_{R1} and J_{R2} as a function of the ratio of the return flow and polar cap ionospheric conductances, α, with $\Sigma_{PC} = 1$ mho. $F_{PC} = 0.5$ GWb, $\Phi_{DD} = 25$ kV, $\theta_D = \theta_N = 30°$, $\Delta\lambda = 9°$.

transport across the dawn-dusk meridian, which we term Φ_{DD}, where

$$\Phi_{DD} = \frac{1}{2}(\Phi_D + \Phi_N) \tag{33}$$

[e.g., *Lockwood*, 1991], indicated in green in Figure 3d. The other measure is the difference between the maximum and minimum potential in the convection pattern, here denoted $\Delta\Phi$, which is typically what is measured by ionospheric radars or other convection-imaging instrumentation, indicated in orange. As discussed by *Milan et al*. [2012], this is the voltage between the ends of the most active merging gap, dayside or nightside, but this is not in general equal to Φ_D or Φ_N as the polar cap is expanding or contracting unless $\Phi_D = \Phi_N$.

[40] Figures 3a and 3b show the simulated R1 and R2 currents from equations (30) and (31) during the 4 h period for the cases where $\Sigma_{PC} = \Sigma_{RF} = 1$ mho and $\Sigma_{PC} = 1$ mho and $\Sigma_{RF} = 4$ mho, respectively. As expected, R1 current is greater than the R2 current at all times; the ratio of R1 to R2 is greatest for $\Sigma_{PC} = \Sigma_{RF}$, decreasing as Σ_{RF} grows relative to Σ_{PC}. The variation of the currents is clearly closely related to Φ_{DD}, which determines the flow shear across the polar cap boundary, and at the equatorward edge of the convection pattern. In addition, there is a weak dependence of the current intensity on the amount of open flux, F_{PC}, and hence the radius of the polar cap.

[41] We examine the influence of the other model parameters on the R1 and R2 current magnitudes in Figures 4–8. In each figure, we calculate J_{R1} and J_{R2} for the cases where the ionospheric conductance is uniform, $\Sigma_{PC} = \Sigma_{RF} = 1$ mho, and where the auroral zone conductance is elevated, $\Sigma_{PC} = 1$ mho, $\Sigma_{RF} = 4$ mho. Unless otherwise stated, we set $\Phi_D = 50$ kV and $\Phi_N = 0$ kV (a modest cross-polar cap potential of $\Phi_{DD} = 25$ kV), $\Delta\lambda = 9°$, $\theta_D = \theta_N = 30°$, and $F_{PC} = 0.5$ GWb.

[42] Figure 4 shows J_{R1} and J_{R2} as a function of the cross-polar cap potential Φ_{DD} (equation (33)). As discussed above, both region 1 and 2 current magnitudes vary linearly with Φ_{DD}, and for a given set of values of Σ_{PC} and Σ_{RF}, the ratio between J_{R1} and J_{R2} remains constant. For the uniform conductance case, $\Sigma_{PC} = \Sigma_{RF} = 1$ mho, this ratio is close to 1.8. In this uniform conductance case, the current magnitudes can be scaled linearly for different values of (uniform) conductance, assuming the other model inputs remain fixed.

[43] In Figure 5, we vary F_{PC} between 0.2 and 1.4 GWb, which is from an extremely contracted polar cap to an extremely expanded one. As suggested above, the current magnitudes increase with increasing F_{PC}, by close to a factor of 2 over the range of F_{PC} modeled, as a consequence of the greater azimuthal distances over which the currents exist.

[44] Figure 6 investigates the effect of changing the latitudinal width of the return flow region, $\Delta\lambda$, between 3° and 15°, from very narrow (though similar in width to that observed by *He et al*. [2012]) to very broad. A narrower return flow region results in a higher current intensity, as the speed of the return flow is higher and the magnitude of the electric field divergence at the poleward and equatorward edges of the region is greater.

[45] Figure 7 shows the effect of varying the widths of the merging gaps, from very narrow convection throats $\theta_D = \theta_N = 10°$ (merging gap width of 20°) to very broad merging regions $\theta_D = \theta_N = 60°$. The variation in current magnitude is less than a factor of 2 but increases for narrower convection throats.

[46] Finally, Figure 8 presents the effect of increasing the ionospheric conductance of the return flow region, Σ_{RF}, with respect to the polar cap, Σ_{PC}. For the modeled case, with $\Sigma_{PC} = 1$ mho, this is also the ratio α (see equations (28)–(31)). As expected, both R1 and R2 current magnitudes increase as the conductance increases. At $\alpha = 1$, the ratio of the R1 to R2 currents is close to 1.4, but this decreases toward 1 as α increases, that is, as current closure across the return flow region becomes increasingly important with respect to that across the polar cap.

4. Discussion

[47] The model presented here allows the azimuthal distribution and overall magnitude of the region 1 and 2 current systems to be estimated in an idealized expanding/contracting polar cap, with differing dayside and nightside reconnection rates, and differing polar cap and return flow region ionospheric conductances. In this section, we discuss the major assumptions made in the model, which impact its limits of applicability, and the implications of the model predictions for solar wind-magnetosphere coupling.

[48] The ECPC [*Cowley and Lockwood*, 1992] recognizes that magnetic reconnection at the low-latitude magnetopause and in the magnetotail change the amount of open flux in the magnetosphere, causing the size of the polar caps to vary and exciting ionospheric convection as part of the Dungey cycle [*Dungey*, 1961, 1963]. The action of reconnection is to open previously closed flux at the dayside edge of the polar cap or to close previously open flux at the nightside boundary, perturbing the shape of the polar cap; however, reconnection does not in itself cause motion of the ionospheric plasma. The reconnection deforms the magnetopause away from magnetohydrostatic equilibrium with the solar wind/magnetosheath flow or causes a reduction of pressure in the magnetotail. Stress imbalances then excite flows in the magnetosphere to return the system to a state of equilibrium, and it is these flows that constitute magnetospheric and ionospheric convection. The flows are such as to return the polar

cap to a roughly circular shape. Although it is not well quantified, it is thought that the flows are excited, and the polar cap returned to a circular shape, on time scales of 10–15 min [e.g., *Khan and Cowley*, 1999, and references therein]. In our model, it is assumed that the ionospheric flows are such as to maintain a circular polar cap at all times; the implications of this assumption will be discussed below.

[49] The region 1 current system is responsible for transmitting stresses from the magnetopause to the ionosphere, and the region 2 current communicates with the inner magnetosphere. Our model computes the field-aligned current necessary to move the ionosphere against the frictional resistance presented by the neutral atmosphere, quantified by the ionospheric conductance. The current is then largely proportional to the strength of convection and the ionospheric conductance. The convection should be largely similar in the Northern and Southern Hemisphere, determined by the ongoing dayside and nightside reconnection rates. As the conductances of the Northern and Southern Hemisphere ionospheres vary seasonally with the level of photoionization, the strength of the Birkeland currents in the two hemispheres should differ, being stronger in the summer hemisphere. This seasonal variation in current intensity has been reported and is consistent with the magnetopause generator of the region 1 current system being a voltage source [*Fujii and Iijima*, 1987], that is, with the convection strength being largely equal in the two hemispheres [e.g., *de la Beaujardiere et al*., 1991; *Ridley*, 2007]. In other words, the currents that flow are dictated by the resistive load of the ionosphere; the magnetopause generator must adjust to provide this current. Polar cap saturation, the phenomenon when Φ_{DD} saturates during periods of very active solar wind-magnetosphere coupling [e.g., *Siscoe et al*., 2002], presumably occurs when the magnetopause generator is not capable of supplying the required current.

[50] The current intensity depends on the cross-polar cap potential Φ_{DD} (equation (33)) but does not depend on the dayside or nightside reconnection rate independently. However, the R1 current maximizes at the ends of the most active merging gap, where the vorticity of the flow is greatest. This implies that the currents should be largest on the dayside during substorm growth phase and should dominate on the nightside during substorm expansion phase. This is consistent with the observations of *Iijima and Potemra* [1978], who studied the R1/R2 FAC dependence on substorm phase. They reported that the R1 current maximized near 1030 and 1300 MLT during quiet periods ($|AL| < 100$ nT), with these maxima shifting toward the nightside (0730 and 1430 MLT, respectively) during active periods ($|AL| > 100$ nT). These observed active-time maxima are not actually located on the nightside (while we might expect maxima near 2100 and 0300 MLT if $\theta_N = 30°$); while this is likely to be due to an over-simplicity of our model, it might also occur because of an imperfect separation of observations into growth phase and expansion phase categories by the activity criterion used by *Iijima and Potemra* [1978].

[51] *Iijima and Potemra* [1978] also reported that the R1/R2 FAC system moved equatorward by 2°–3° of latitude during active periods (defined as above), consistent with the expanding/contracting nature of the polar cap. The FAC intensities were shown to increase during active periods, consistent with average substorm values of Φ_N exceeding the average value of Φ_D [*Milan et al*., 2007], and the possibility that Φ_D is nonzero during substorm expansion phase, leading to large values of Φ_{DD}. Finally, *Iijima and Potemra* [1978] reported that the R1/R2 current regions broadened in latitude by 20–30% during active periods; this could be reproduced in the model by requiring that $\Delta\lambda$ should increase when Φ_N is nonzero.

[52] The model assumes that the polar cap remains circular. In the real world, significant deviations of the polar cap from a circular shape occur during intense substorms when the conductivity of the auroral bulge becomes sufficiently high that frictional coupling with the atmosphere retards ionospheric motions [e.g., *Morelli et al*., 1995]. Variations in conductance associated with, e.g., substorms are not considered in the model, and the assumption that the polar cap remains circular implicitly assumes that the conductance remains sufficiently low that the retardation of ionospheric motions is negligible. As reported by *Grocott et al*. [2009], flow retardation is most likely to occur during substorms occurring on an expanded auroral oval as these substorms are associated with the most intense precipitation [*Milan et al*., 2009].

[53] For mathematical simplicity, the model assumes that the ionospheric conductance is uniform (though allowing different conductances in the polar cap and return flow regions). However, if, as above, it is assumed that the conductance does not modify the ionospheric flow pattern, then any conductance model can be implemented. Modifications of the model could be made to allow for increased conductance in the dayside ionosphere, or changes in auroral zone conductance for different phases of the substorm cycle.

[54] The model does not include the formation of a substorm current wedge during substorms, due to current disruption in the tail and the modification of the field-aligned currents that this would entail [*Atkinson*, 1967; *McPherron et al*., 1973]. Nor does it include field-aligned currents associated with the Harang discontinuity [*Kunkel et al*., 1986], which are thought to be the result of a dawn-dusk pressure gradient in the central plasma sheet [*Erickson et al*., 1991]. The ionospheric convection pattern is known to develop dawn-dusk asymmetries when the IMF has a nonzero B_Y component. These asymmetries will lead to dawn-dusk asymmetries in the field-aligned currents, but this is not accounted for in the model. Nor do we consider the formation of the NBZ current system at the dayside when the IMF is directed northward, and reverse convection is expected within the polar cap [e.g., *Milan et al*., 2000].

[55] Despite the assumptions and limitations of the model, it can be used gainfully to understand the factors that determine region 1 and 2 current intensities and, most importantly, the dynamics of the current systems under different solar wind-magnetosphere coupling conditions. These include changes in the latitude of the current regions as the polar caps expand and contract and the local time of the current maxima as dayside and nightside reconnection rates vary. Most previous studies of the current systems have relied on empirical models derived from averages of multiple spacecraft orbits. Although these can be parameterized by, e.g., interplanetary magnetic field orientation and strength [e.g., *Weimer*, 2005; *Anderson et al*., 2008; *He et al*., 2012], they have not been able to investigate dynamics on short time scales such as the substorm cycle. The advent of

the AMPERE technique [e.g., *Anderson et al*., 2000, 2002; *Clausen et al*., 2012] allows the configuration of the current systems to be determined at 10 min cadence in both Northern and Southern Hemispheres. The expanding/contracting nature of the current systems has already been demonstrated [*Clausen et al*., 2012]. It is to interpretation of this data set that our model will be particularly applicable.

[56] In principle, the model could be extended to compute the Hall currents from equations (3) and (26), using a suitable assumption about the nature of Σ_H (similar to Σ_P), from which the magnetic perturbation on the ground could be determined, allowing synthetic *AU* and *AL* indices to be constructed. This would not include AL bays associated with substorms (see discussion above), but could provide an additional means of constraining the model with respect toreal-world observations. A related problem is the derivation of the ionospheric Pedersen conductance pattern from combined observations of the field-aligned currents (e.g., using AMPERE) and the ionospheric convection pattern (e.g., using the Super Dual Auroral Radar Network [e.g., *Chisham et al*., 2007]). Although such a data assimilation method is considerably beyond the scope of the present paper, it is possible that the analytical model presented here could form the framework within which such an assimilation could be attempted.

5. Conclusions

[57] We have presented a simple mathematical model of the expected region 1 and 2 field-aligned current intensities consistent with changing dayside and nightside reconnection rates and the expanding/contracting polar cap paradigm. The currents are shown to be related to the mean of the dayside and nightside reconnection rates, otherwise known as the cross-polar cap potential or transpolar voltage. However, the greatest current intensities should appear in the dayside or nightside regions, depending on whether dayside or nightside reconnection dominates. In other words, when the polar cap is expanding, current intensities should be enhanced on the dayside, while currents should be greatest on the nightside when the polar cap is contracting. The model also predicts that current intensities should increase if the merging gaps are narrower, the ionospheric convection return flow regions are narrower, and when the polar cap is expanded. It is thought that all of these characteristics are broadly consistent with previous observations of the R1/R2 FAC system.

[58] **Acknowledgments.** The author would like to acknowledge the International Space Science Institute, Bern, Switzerland, for providing the convivial surroundings in which some of the work presented in this paper was prepared. The work was supported by STFC grant ST/H002480/1. I would also like to thank L. B. N. Clausen and J. C. Coxon for stimulating discussions regarding AMPERE observations of the Birkeland current systems.

[59] Robert Lysak thanks Kathryn McWilliams and another reviewer for their assistance in evaluating this paper.

References

Amm, O. (1995), Direct determination of the local ionospheric Hall conductance distribution from two-dimensional electric and magnetic field data: Application of the method using models of typical ionospheric electrodynamic situations, *J. Geophys. Res.*, *100*, 21,473–21,488, doi:10.1029/95JA02213.

Anderson, B. J., K. Takahashi, and B. A. Toth (2000), Sensing global Birkeland currents with Iridium® engineering magnetometer data, *Geophys. Res. Lett.*, *27*, 4045–4048, doi:10.1029/2000GL000094.

Anderson, B. J., K. Takahashi, T. Kamei, C. L. Waters, and B. A. Toth (2002), Birkeland current system key parameters derived from Iridium observations: Method and initial validation results, *J. Geophys. Res.*, *107*(A6), 1079, doi:10.1029/2001JA000080.

Anderson, B. J., H. Korth, C. L. Waters, D. L. Green, and P. Stauning (2008), Statistical Birkeland current distributions from magnetic field observations by the Iridium® constellation, *Ann. Geophys.*, *26*, 671–687, doi:10.5194/angeo-26-671-2008.

Atkinson, G. (1967), An approximate flow equation for geomagnetic flux tubes and its application to polar substorms, *J. Geophys. Res.*, *72*, 5373–5382.

Birkeland, K. (1908), *The Norwegian Aurora Polaris Expedition 1902–1903*, vol. *1*, H. Aschehoug, New York and Christiania.

Chisham, G., et al. (2007), A decade of the Super Dual Auroral Radar Network (SuperDARN): Scientific achievements, new techniques and future directions, *Surv. Geophys.*, *28*, 33–109, doi:10.1007/s10712-007-9017-8.

Chisham, G., et al. (2008), Remote sensing of the spatial and temporal structure of magnetopause and magnetotail reconnection from the ionosphere, *Rev. Geophys.*, *46*, RG1004, doi:10.1029/2007RG000223.

Chisham, G., M. P. Freeman, G. A. Abel, W. A. Bristow, A. Marchaudon, J. M. Ruohoniemi, and G. J. Sofko (2009), Spatial distribution of average vorticity in the high-latitude ionosphere and its variation with interplanetary magnetic field direction and season, *J. Geophys. Res.*, *114*, A09301, doi:10.1029/2009JA014263.

Clausen, L. B. N., J. B. H. Baker, J. M. Ruohoniemi, S. E. Milan, and B. J. Anderson (2012), Dynamics of the region 1 Birkeland current oval derived from the Active Magnetosphere and Planetary Electrodynamics Response Experiment (AMPERE), *J. Geophys. Res.*, *117*, A06233, doi:10.1029/2012JA017666.

Cowley, S. W. H. (2000), Magnetosphere-ionosphere interactions: A tutorial review, in *Magnetospheric Current Systems, Geophys. Monogr. Ser.*, vol. *118*, edited by S. Ohtani et al., pp. 91–106, AGU, Washington, D. C., doi:10.1029/GM118p0091.

Cowley, S. W. H., and M. Lockwood (1992), Excitation and decay of solar wind-driven flows in the magnetosphere-ionosphere system, *Ann. Geophys.*, *10*, 103–115.

De La Beaujardiere, O., D. Alcayde, J. Fontanari, and C. Leger (1991), Seasonal dependence of high-latitude electric fields, *J. Geophys. Res.*, *96*, 5723–5735.

Dungey, J. W. (1961), Interplanetary magnetic fields and the auroral zones, *Phys. Rev. Lett.*, *6*, 47–48.

Dungey, J. W. (1963), The structure of the exosphere or adventures in velocity space, in *Geophysics, The Earth's Environment*, edited by C. De Witt, J. Hieblot, and L. Le Beau, p. 503–550, Gordon and Breach, New York.

Erickson, G. M., R. W. Spiro, and R. A. Wolf (1991), The physics of Harang discontinuity, *J. Geophys. Res.*, *96*, 1633–1645.

Freeman, M. P. (2003), A unified model of the response of ionospheric convection to changes in the interplanetary magnetic field, *J. Geophys. Res.*, *108*(A1), 1024, doi:10.1029/2002JA009385.

Freeman, M. P., and D. J. Southwood (1988), The effect of magnetospheric erosion on mid- and high-latitude ionospheric flows, *Planet. Space Sci.*, *36*(509–522), 1988.

Fujii, R., and T. Iijima (1987), Control of the ionospheric conductivities on large-scale Birkeland current intensities under geomagnetic quiet conditions, *J. Geophys. Res.*, *92*, 4505–4513.

Fujii, R., R. A. Hoffman, P. C. Anderson, J. D. Craven, M. Sugiura, L. A. Frank, and N. C. Maynard (1994), Electrodynamic parameters in the nighttime sector during auroral substorms, *J. Geophys. Res.*, *99*(A4), 6093–6112, doi:10.1029/93JA02210.

Grocott, A., J. A. Wild, S. E. Milan, and T. K. Yeoman (2009), Superposed epoch analysis of the ionospheric convection evolution during substorms: onset latitude dependence, *Ann. Geophys.*, *27*, 591–600.

He, M., J. Vogt, H. Lühr, E. Sorbalo, A. Blagau, G. Le, and G. Lu (2012), A high-resolution model of field-aligned currents through empirical orthogonal functions analysis (MFACE), *Geophys. Res. Lett.*, *39*, L18105, doi:10.1029/2012GL053168.

Hoffman, R. A., R. Fujii, and M. Sugiura (1994), Characteristics of the field-aligned current system in the nighttime sector during auroral substorms, *J. Geophys. Res.*, *99*(A11), 21,303–21,325, doi:10.1029/94JA01659.

Iijima, T., and T. A. Potemra (1976a), The amplitude distribution of field-aligned currents at northern high latitudes observed by Triad, *J. Geophys. Res.*, *81*, 2165–2174, doi:10.1029/JA081i013p02165.

Iijima, T., and T. A. Potemra (1976b), Field-aligned currents in the dayside cusp observed by Triad, *J. Geophys. Res.*, *81*, 5971–5979, doi:10.1029/JA081i034p05971.

Iijima, T., and T. A. Potemra (1978), Large-scale characteristics of field-aligned currents associated with substorms, *J. Geophys. Res.*, *83*, 599–615.

Khan, H., and S. W. H. Cowley (1999), Observations of the response time of the high-latitude ionospheric convection to variations in the interplanetary

magnetic field using EISCAT and IMP-8 data, *Ann. Geophys.*, *17*, 1306–1335.

Kunkel, T., W. Baumjohann, J. Untiedt, and R. Greenwald (1986), Electric fields and currents at the Harang discontinuity: A case study, *J. Geophys.*, *59*, 73–86.

Lockwood, M. (1991), On flow reversal boundaries and transpolar voltage in average models of high latitude convection, *Planet. Space Sci.*, *3*, 397–409.

Lockwood, M., and S. W. H. Cowley (1992), Ionospheric convection and the substorm cycle, in Proceedings of the International Conference on Substorms (ICS-1), pp. 99–109, ESA Noordwijk, The Netherlands.

McPherron, R. L., C. T. Russell, and M. Aubry (1973), Satellite studies of magnetospheric substorms on August 15, 1978: 9. Phenomenological model for substorms, *J. Geophys. Res.*, *78*, 3131–3149.

McWilliams, K. A. (1997), A SuperDARN study of dayside field-aligned current regions, MSc thesis, Univ. of Saskatchewan, Saskatoon, Sask., Canada.

Milan, S. E., M. Lester, S. W. H. Cowley, and M. Brittnacher (2000), Dayside convection and auroral morphology during an interval of northward interplanetary magnetic field, *Ann. Geophys.*, *18*, 436–444.

Milan, S. E., M. Lester, S. W. H. Cowley, K. Oksavik, M. Brittnacher, R. A. Greenwald, G. Sofko, and J.-P. Villain (2003), Variations in polar cap area during two substorm cycles, *Ann. Geophys.*, *21*, 1121–1140.

Milan, S. E., G. Provan, and B. Hubert (2007), Magnetic flux transport in the Dungey cycle: A survey of dayside and nightside reconnection rates, *J. Geophys. Res.*, *112*, A01209, doi:10.1029/2006JA011642.

Milan, S. E., A. Grocott, C. Forsyth, S. M. Imber, P. D. Boakes, and B. Hubert (2009), A superposed epoch analysis of auroral evolution during substorm growth, onset and recovery: Open magnetic flux control of substorm intensity, *Ann. Geophys.*, *27*, 659–668.

Milan, S. E., J. S. Gosling, and B. Hubert (2012), Relationship between interplanetary parameters and the magnetopause reconnection rate quantified from observations of the expanding polar cap, *J. Geophys. Res.*, *117*, A03226, doi:10.1029/2011JA017082.

Morelli, J. P., et al. (1995), Radar observations of auroral zone flows during a multiple-onset substorm, *Ann. Geophys.*, *13*, 1144–1163, doi:10.1007/s00585-995-1144-2.

Opgenoorth, H. J., R. J. Pellinen, H. Maurer, F. Küppers, W. J. Heikkilä, K. U. Kaila, and P. Tanskanen (1980), Ground-based observations of an onset of localized field-aligned currents during auroral break-up around magnetic midnight, *J. Geophys.*, *48*, 101–115.

Ridley, A. J. (2007), Effects of seasonal changes in the ionospheric conductances on magnetospheric field-aligned currents, *Geophys. Res. Lett.*, *34*, L05101, doi:10.1029/2006GL028444.

Rostoker, G., S.-I. Akasofu, J. Foster, R. A. Greenwald, Y. Kamide, K. Kawasaki, A. T. Y. Lui, R. L. McPherron, and C. T. Russell (1980), Magnetospheric substorms—Definition and signatures, *J. Geophys. Res.*, *85*, 1663–1668.

Siscoe, G. L., and T. S. Huang (1985), Polar cap inflation and deflation, *J. Geophys. Res.*, *90*, 543–547.

Siscoe, G. L., N. U. Crooker, and K. D. Siebert (2002), Transpolar potential saturation: Roles of region 1 current system and solar wind ram pressure, *J. Geophys. Res.*, *107*(A10), 1321, doi:10.1029/2001JA009176.

Sofko, G. J., R. Greenwald, and W. Bristow (1995), Direct determination of large-scale magnetospheric field-aligned currents with SuperDARN, *Geophys. Res. Lett.*, *22*, 2041–2044.

Weimer, D. R. (2005), Improved ionospheric electrodynamic models and application to calculating Joule heating rates, *J. Geophys. Res.*, *110*, A05306, doi:10.1029/2004JA010884.

Zmuda, A. J., J. H. Martin, and F. T. Heuring (1966), Transverse magnetic disturbances at 1100 kilometres in the auroral region, *J. Geophys. Res.*, *71*, 5033–5045.